

A Preliminary *Chandra* X-ray Spectroscopy of the Supernova Remnant N132D

Xiao Xiao, Yang Chen

Department of Astronomy, Nanjing University, Nanjing 210093, P.R.China

Abstract

We present the preliminary results of a *Chandra* X-ray study of N132D, a young shell-like supernova remnant (SNR) in the Large Magellanic Cloud. The equivalent width maps of emissions from O, Ne, Mg, Si, and S are provided. Spatially resolved spectral analysis for the small-scale regions were tentatively performed. The X-ray spectra of the interior can be described with a single-thermal model. The faint interior regions have lower density and higher temperature (above 1keV) than those of bright interior regions. The X-ray spectra along the shell can be phenomenally fitted with either a double-*vphshock* model or a *vphshock* + *powerlaw* model. If the non-thermal component is true, N132D would be listed as another X-ray synchrotron SNR.

Key words: ISM, Supernova remnants, N132D, X-rays, Large Magellanic Cloud

1 Introduction

N132D, one of the prototype O-rich supernova remnants (SNRs) of a massive progenitor, is located in the bar of the Large Magellanic Cloud (LMC) (Danziger & Dennefeld, 1976; Lasker, 1978). In X-ray morphology, N132D is an irregular shell of radius about 50'' with a break-out in the northeast (Mathewson et al., 1983). N132D is a good object to test the stellar evolution and nucleosynthesis models of massive stars since the interior fragments are exposed to direct investigation (Blair et al., 2000). N132D has two advantages for observation. First, because it is located in the LMC, the distance is well determined (50kpc) and the extinction is low. Second, N132D is one of the brightest soft X-ray sources in the LMC (Favata et al., 1997). Multi-band observations have been performed on it.

In X-rays, Hwang et al. (1993) obtained relatively high resolution spectrum of N132D with the Einstein Solid State Spectrometer. Emission lines of O^{6+} , O^{7+} ,

Ne^{9+} , and Fe^{16+} were detected. In their work, the best-fit element abundances derived with a single-temperature non-equilibrium ionization (NEI) model are lower than the LMC mean abundances. With the data obtained by the concentrator spectrometer on board the X-ray satellite BeppoSAX, Favata et al. (1997, 1998) found that there should be two components with temperatures of 3.3keV and 0.79keV respectively. The element abundances derived with the two thermal components model are similar to the normal LMC abundances. Hughes et al. (1998) first reported the CCD data of N132D obtained by the Solid State Imaging Spectrometer on board the Advanced Satellite for Cosmology and Astrophysics (ASCA). They fitted the ASCA data of high resolution with a single Sedov model and found that the temperature is around 0.7keV and the element abundances are all around the LMC mean, too. Based on the ASCA observation, Chen et al. (2003) modeled the remnant evolution as the blast wave hitting the pre-existing cavity wall. With the extremely high spectral resolution of the Reflection Grating Spectrometers on board the XMM-Newton X-ray observatory, Behar et al. (2001) detected lines of C, N, O, Ne, Mg, Si, S, Ar, Ca, and Fe in the spectrum of N132D. Images in the narrow wave-length bands show that, with the exception of O, the dominant part of the soft X-ray emission originates from shocked interstellar medium (ISM). Using High Energy Transmission Grating (HETG) on board Chandra, Canizares et al. (2001) got dispersed high resolution X-ray images of N132D in which some regions of oxygen-rich material were clearly identified despite the spatial/spectral overlap.

In the optical and UV bands, with IUE data, Blair et al. (1994) noted that the X-ray peaks near the center were generally associated with low-velocity, normal composition, optical filaments, rather than with high-velocity, oxygen-rich ones. Morse et al. (1996) obtained high spatial resolution images of N132D with Hubble Space Telescope (HST). They distinguished oxygen-rich filaments from shocked clouds. Comparing with the ROSAT images, they confirmed that the O-rich ejecta emit little X-rays. Blair et al. (2000) performed detailed spectral analysis on the data from HST. The abundance they derived from the shocked ISM cloud in N132D is consistent with the LMC mean. From the spectra of the O-rich ejecta they clearly detected O, C, Ne, and Mg lines, but found no evidence of O-burning elements. They suggested that N132D is the remnant of a Type Ib supernova explosion of a W/O progenitor star with extensive O-rich mantle.

In radio, Dickel & Milne (1995) found that the 6 cm radio emission from N132D largely coincide with the X-ray shell, in other words the shell of N132D seems to be the source of both X-ray and synchrotron radio emission.

Recently, Tappe et al. (2006) detected strong 24 μm infrared emission from swept-up, shock-heated dust grains in the N132D with Spitzer Space Telescope. The image of 24 μm emission follows the X-ray image well. Additionally,

they detected PAH molecular bands from N132D.

Profited from the high spatial resolution of Chandra, we have performed a spatially resolved spectroscopic analysis of N132D and present a fresh look of the physical properties of the remnant.

2 Observation and Data Analysis

We combined two sets of data (ObsId 121 and 1821 observed by C.R. Canizares) released by Chandra X-ray center. Both of the data were dispersed by the HETG at first, then read out by the Advanced CCD Imaging Spectrometer (ACIS). The two observations were carried out on 2000 July 19 with exposure time of 22ks and on 2000 July 20 with exposure time of 74 ks, respectively.

The tool we used to process the data is Chandra Interactive Analysis of Observations (CIAO) software package (ver. 3.2). Considering the effect of the spatial/spectral overlap after dispersion by the HETG, we only analyzed the zeroth order data. The two sets of data were reprocessed separately to generate level 2 event files following the threads for extended sources (the threads are available on <http://cxc.harvard.edu/ciao/>). During the course of the reprocessing, we corrected hot pixels and cosmic ray afterglows, filtered bad grades and applied good time intervals correction. Then we merged the two sets of cleaned data for subsequent analysis.

2.1 Spatial Analysis

Fig.1 shows diffuse emission from SNR N132D in the broad band 0.3-8.0 keV. Regions shown in the map are used for spectral analysis (see section 2.2). This image displays a horseshoe morphology with a bright ridge south to the center, similar to that found in earlier X-ray observations (Mathewson et al., 1983; Hughes, 1987; Behar et al., 2001) as well as the recent IR observation (Tappe et al., 2006). It is easy to distinguish a bright shell with a break-out in the northeast. Noticeably, there are some bright knots and thin filaments along the shell.

The tricolor X-ray image is shown in Fig.2. The 0.3-1.0keV emission is coded in red, 1.0-2.0keV in green, and 2.0-8.0keV in blue. The images in the three bands were adaptively smoothed using CIAO tool *csmooth* with a signal-to-noise ratio of 3 respectively. In the tricolor image, soft emission (in red) is basically observed all over the image. Soft emission dominates the northeast region where the break-out locates. Southwestward, the proportion of hard

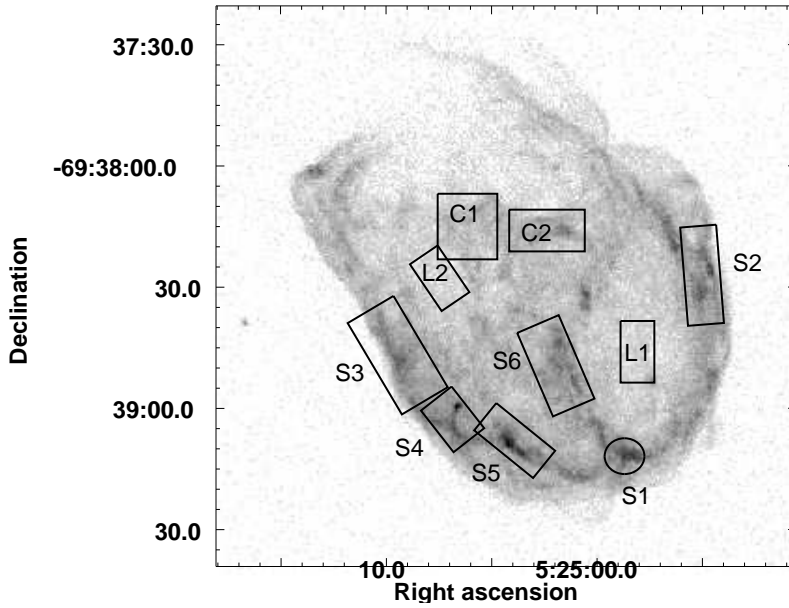


Fig. 1. Raw ACIS-S image of N132D in square-root brightness scales. The labeled regions are used for spectrum extraction.

emission (in blue) increases. Hard emission could be easily distinguished in the south part of the horseshoe-like shell.

From the overall spectrum of N132D (Fig.3), we can distinguish emission lines of element species O, Ne, Mg, Si, S, Ar, Ca, and Fe, as are seen in the XMM spectrum (Behar et al., 2001). Considering the low signal-to-noise ratio in the high energy band, we only present the equivalent width (EW) maps of O, Ne, Mg, Si, and S. Here we have applied an adaptive mesh method to rebin the data so as to include at least 10 counts in each bin. EW map indicates regions of high line to continuum ratio, which varies with element abundances, temperature, ionization parameter, and even column density (Hwang et al., 2000).

The EW of O (left panel of Fig.4) is high in the north near the breakout. In this map, we also see a shell which follows the X-ray intensity shell but is thinner than it. The EW of Ne (right panel of Fig.4) is comparatively uniform across the SNR except for some bright knots along/near the shell. The strength distribution of Mg EW (left panel of Fig.5) follows the X-ray intensity image well but it seems to have smaller extent than that of O and Ne, especially in the north. The EW of Si (right panel of Fig. 5) is fairly uniform, but the EW in an interior patch around $(05^{\text{h}}25^{\text{m}}04^{\text{s}}, -69^{\circ}38'24'')$ is roughly twice as high as the average. The EW of S (Fig. 6) is enhanced in the intensity shell and an interior patch near the center.

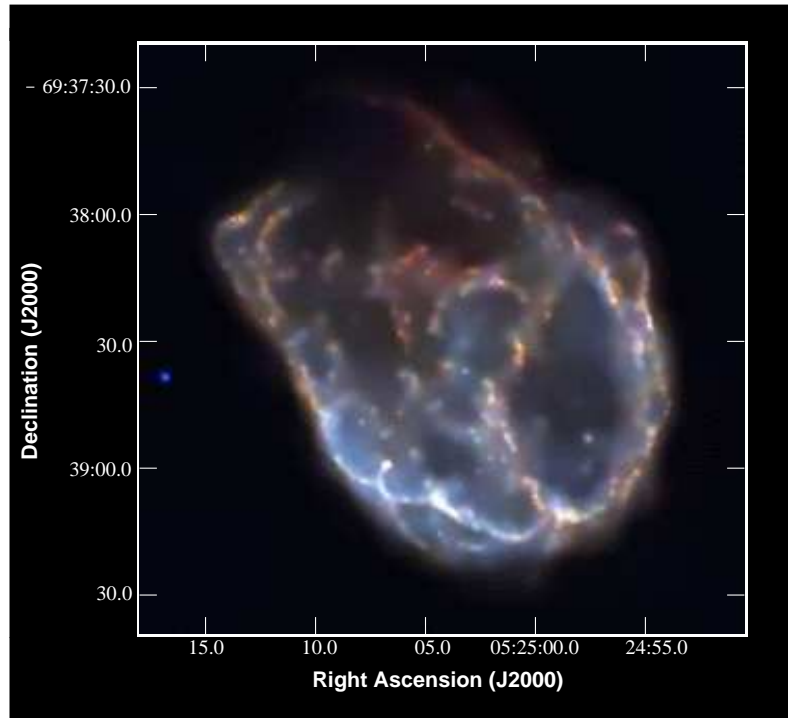


Fig. 2. Tricolor X-ray image of N132D: red color represents 0.3-1.0keV emission, green color represents 1.0-2.0keV emission, and blue color represents 2.0-8.0keV emission.

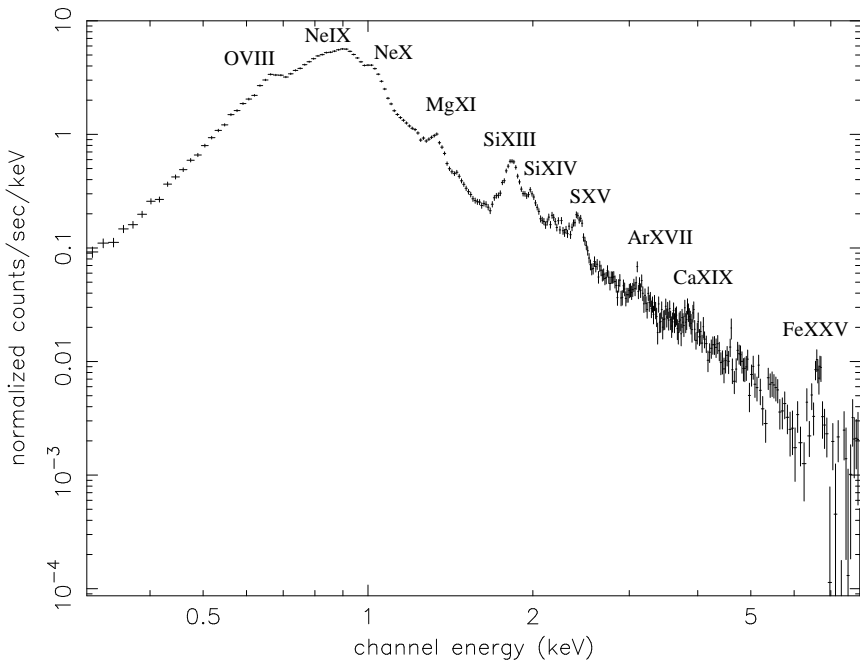


Fig. 3. The overall spectrum of N132D with the major emission lines labeled

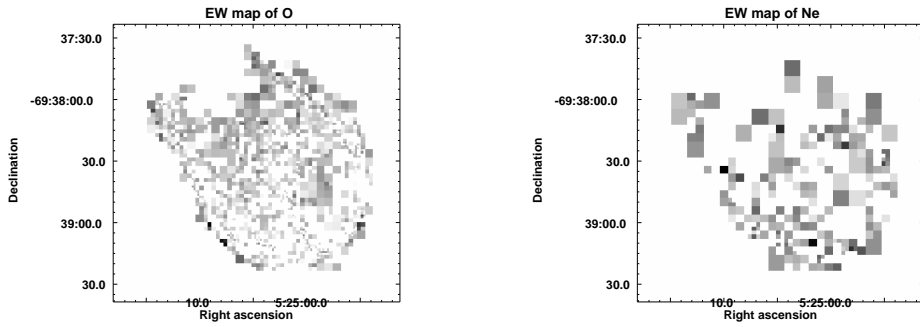


Fig. 4. Left panel: the EW map of O line at 0.65keV. Right panel: the EW map of Ne line at 1.02keV. Both maps are in square-root brightness scales.

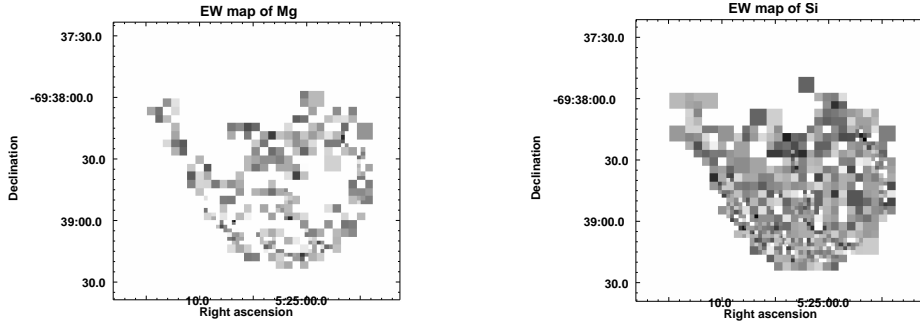


Fig. 5. Left panel: the EW map of Mg line at 1.34keV. Right panel: the EW map of Si line at 1.87keV. Both maps are in square-root brightness scales.

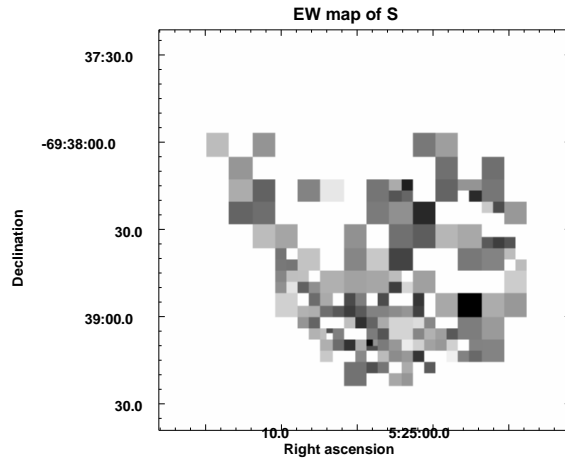


Fig. 6. The EW map of S line at 2.45keV in square-root brightness scales.

2.2 Spectral Analysis

The overall spectrum of N132D is shown in Fig.3, which shows line features of OVIII (~ 0.65 keV), NeIX (~ 0.92 keV), NeX (~ 1.02 keV), MgXI (~ 1.34 keV), SiXIII (~ 1.87 keV), SiXIV (~ 2.0 keV), SXV (~ 2.45 keV), ArXVII (~ 3.12 keV), CaXIX (~ 3.86 keV), and FeXXV K_{α} (~ 6.65 keV). Due to its complexity, at least two components are needed to fit the spectrum. Profited from Chandra's superb angular resolution, we could perform spatially resolved spectral analysis of N132D. We defined 10 small-scale regions (diagrammed in Fig.1) for spectral investigation. Regions S1, S2, S3, S4, and S5 are located along the shell, and region S6 includes a part of the bright ridge; C1 and C2 represent two bright interior regions; L1 and L2 represent two faint interior regions. A nearby region which is not affected by photons from N132D was selected as background. We extracted spectrum from each region using CIAO script *acissspec*. All the spectra mentioned above were regrouped to contain at least 25 net counts per bin. The spectra were analyzed with software Xspec (ver. 11.3.1).

We fit the spectra of the small-scale regions with absorbed NEI plane-parallel shock model *vpshock* and/or the power law model *powerlaw*. We use the cross-sections of Morrison & McCammon (1983) and assume solar abundances. The spectral fit allows the abundances of the significant line-emitting elements to vary, while other metal abundances are set to 0.3 solar, typical for the LMC (Russell & Dopita, 1992). The thermal NEI model *vpshock* provides the plasma temperature kT , the ionization timescale $n_e t$, and the normalization parameter $norm = \frac{10^{-14}}{4\pi d^2} \int n_e n_H dV$, where d is the distance to the source, n_e and n_H are the electron density and the hydrogen density respectively, and V is the volume of the region. Approximatively $norm = \frac{10^{-14}}{4\pi d^2} f n_e n_H V$, where f is the filling factor. Volumes of the shell regions (S2-S5) are calculated as the intersection of a sphere (the remnant) and columns. Shell region S1 is assumed to be an oblate spheroid. The rectangular regions C1, C2, L1, L2, and S6 are approximated as cuboids with average line-of-sight size to be the remnant radius R . Using $n_e \approx 1.2 n_H$, we can estimate the density $n_H/f^{-1/2}$ from parameter *norm*.

The spectra from interior regions C1, C2, L1, and L2 can be described well with a single-*vpshock* model. Results are given in Table 1. In the faint regions L1 and L2, the temperature is above 1keV and the abundances of heavy elements are higher than the LMC mean while in the bright regions C1 and C2, the temperature is below 1keV and the abundances are close to the LMC mean. The $n_H/f^{-1/2}$ values of C1 and C2 are almost twice/thrice those of L1 and L2.

For the spectra of regions S1-S6, one component model is not enough to get

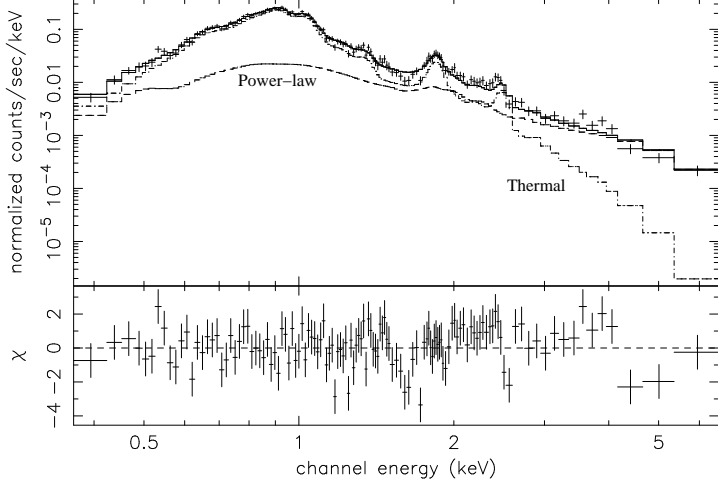


Fig. 7. ACIS-S spectrum of shell region S4 fitted with *vpshock+powerlaw* model. The two spectral components are also drawn separately. The lower panel shows the residuals of the data minus the model in units of σ .

an acceptable fit (spectrum of S4 for example in Fig.7). We found that there is always a hard energy tail above 2keV band which can not be fit well with only one thermal model. Therefore we tentatively fit these spectra with two components.

As the first possibility, the complex spectra may include two thermal components of different temperatures. We tried to fit the spectra with double-*vpshock* model. Abundances of O, Si, S, and Fe of the hot components were thawed. The χ^2 value is acceptable and the results are given in Table 2. The temperatures of the cool components are around 0.5-0.6keV while the temperatures of the hot component are around 1.5keV. Some element abundances in S4 and S5 are slightly overabundant. The parameters derived from the ridge-like region S6 are similar to those derived from the shell regions except for the element abundances which are close to the average abundance of the LMC. The ionization timescale $n_e t$ of the cool components are high ($\geq 10^{12} \text{ cm}^{-3} \text{ s}$) in all regions (S1-S6) except S4. Parameter $n_{\text{H}}/f^{-1/2}$ of the cool components is almost twice/thrice those of hot components. We also tried the two-component model with equal abundances. The temperatures and ionization timescales are similar to those we present here. The abundances of the "equal" model are similar to those of the hot component in the presented model within their errors. The problems of the two thermal components models will be discussed in section 3.2.

Another possibility is that the spectra contain a non-thermal component in addition to a thermal one. We fit the spectra with *vpshock + powerlaw* model (spectrum of S4 for example in Fig.7) and tabulate the results in Table 3. The photon indices are between 2.3 and 3.4. The temperatures of the thermal components are around 0.6keV. In the shell regions (S1-S5), some element

Table 1

VPSHOCK fitting results with 90% confidence ranges and estimates of the gas density for interior regions

Region	L1	L2	C1	C2
$N_{\text{H}}(10^{21} \text{ cm}^{-2})$	$1.9_{-1.0}^{+1.3}$	$1.3_{-0.9}^{+1.1}$	$0.8_{-0.3}^{+0.4}$	$0.9_{-0.3}^{+0.3}$
$kT(\text{keV})$	$1.65_{-0.44}^{+1.13}$	$1.20_{-0.32}^{+0.58}$	$0.79_{-0.10}^{+0.11}$	$0.83_{-0.10}^{+0.15}$
$norm(10^{-4})$	$2.10_{-2.10}^{+1.20}$	$2.48_{-1.17}^{+1.74}$	$18.55_{-4.58}^{+6.31}$	$21.52_{-5.87}^{+4.40}$
$n_e t(10^{11} \text{ cm}^{-3} \text{ s})$	$1.10_{-0.43}^{+0.90}$	$1.23_{-0.51}^{+1.21}$	$1.02_{-0.30}^{+0.55}$	$1.09_{-0.39}^{+0.62}$
O	$1.56_{-0.80}^{+2.33}$	$0.82_{-0.43}^{+0.69}$	$0.37_{-0.06}^{+0.09}$	$0.26_{-0.10}^{+0.07}$
Ne	$0.3(frozen)$	$0.3(frozen)$	$0.53_{-0.08}^{+0.10}$	$0.35_{-0.07}^{+0.11}$
Si	$0.93_{-0.39}^{+1.75}$	$0.42_{-0.30}^{+0.38}$	$0.26_{-0.11}^{+0.12}$	$0.28_{-0.08}^{+0.13}$
S	$0.3(frozen)$	$0.3(frozen)$	$0.3(frozen)$	$1.02_{-0.40}^{+0.55}$
Fe	$1.20_{-0.50}^{+1.59}$	$0.72_{-0.33}^{+0.80}$	$0.23_{-0.05}^{+0.08}$	$0.36_{-0.03}^{+0.11}$
<i>net count rate</i>				
$(10^{-2} \text{ counts s}^{-1})$	1.81 ± 0.04	1.48 ± 0.04	7.00 ± 0.09	8.02 ± 0.09
$\chi^2/\text{d.o.f.}$	1.24	1.12	1.10	1.30
$F^{(0)}(0.3\text{-}8 \text{ keV})$				
$(10^{-11} \text{ ergs cm}^{-2} \text{ s}^{-1})$	0.168	0.120	0.579	0.627
$V(10^{57} \text{ cm}^3)$	2.51	2.13	4.71	3.80
$n_{\text{H}}/f^{-1/2}(\text{cm}^{-3})$...	1.44	1.70	3.12	3.74

abundances in some regions especially S4 and S5 are slightly overabundant. The parameters of S6 are similar to those of the shell regions again except for the element abundances which are close to the LMC mean.

3 Discussion

3.1 The interior regions

For the interior regions that have been spectrally analyzed, we find that the faint regions L1 and L2 have higher temperature (above 1keV) and overabundant heavy elements while interior bright regions C1 and C2 have lower temperature (below 1keV) and lower abundances close to the LMC mean. We note that parameter $n_{\text{H}}/f^{-1/2}$ derived from the volume emission measure of the gas in the bright regions is about twice/thrice those in the faint regions. The products of n_{H} and kT for these regions are around $2.4f^{-1/2} \text{ cm}^{-3} \text{ keV}$, suggesting that the cool dense regions may be in pressure balance with the hot tenuous regions (given that the filling factors are similar).

Table 2

VPSHOCK+VPSHOCK fitting results with 90% confidence ranges and estimates of the gas density for regions S1-S6

Region	<i>S1</i>	<i>S2</i>	<i>S3</i>	<i>S4</i>	<i>S5</i>	<i>S6</i>
$N_{\text{H}}(10^{21} \text{ cm}^{-2})$	$1.7^{+0.4}_{-1.0}$	$1.5^{+0.5}_{-0.5}$	$1.1^{+0.2}_{-0.2}$	$1.4^{+0.3}_{-0.3}$	$1.5^{+0.3}_{-0.2}$	$1.9^{+0.7}_{-0.6}$
<i>net count rate</i>						
$(10^{-2} \text{ counts s}^{-1})$	8.47 ± 0.09	14.73 ± 0.13	18.87 ± 0.14	12.64 ± 0.12	15.45 ± 0.13	17.16 ± 0.14
$\chi^2/\text{d.o.f.}$	1.14	1.60	1.55	1.38	1.03	1.49
$F^{(0)}(0.3\text{-}8 \text{ keV})$						
$(10^{-11} \text{ ergs cm}^{-2} \text{ s}^{-1})$	0.729	1.25	1.22	0.904	1.12	1.58
$V(10^{57} \text{ cm}^3)$	0.19	4.64	9.81	5.37	3.19	4.94
Cool Component						
$kT_c(\text{keV})$	$0.53^{+0.05}_{-0.13}$	$0.42^{+0.11}_{-0.03}$	$0.63^{+0.03}_{-0.03}$	$0.62^{+0.06}_{-0.05}$	$0.59^{+0.04}_{-0.03}$	$0.41^{+0.14}_{-0.07}$
$norm(10^{-4})$	$40.22^{+10.88}_{-10.87}$	$71.83^{+22.75}_{-21.34}$	$57.94^{+4.31}_{-10.55}$	$37.87^{+6.08}_{-6.60}$	$53.92^{+4.77}_{-5.49}$	$86.86^{+73.74}_{-26.35}$
$n_{et}(10^{11} \text{ cm}^{-3} \text{ s})$	$7.41(> 5.03)$	$11.0(> 9.32)$	$500(> 391)$	$6.39^{+7.72}_{-2.37}$	$498(> 423)$	$83.2(> 25.2)$
$n_{\text{H}}/f^{-1/2}(\text{cm}^{-3})$	22.78	6.19	3.82	4.17	6.47	6.59
Hot Component						
$kT_h(\text{keV})$	$1.65^{+1.19}_{-0.55}$	$1.36^{+0.24}_{-0.15}$	$1.59^{+0.23}_{-0.21}$	$1.73^{+0.36}_{-0.24}$	$1.53^{+0.32}_{-0.07}$	$1.35^{+0.18}_{-0.12}$
$norm(10^{-4})$	$4.24^{+8.68}_{-2.88}$	$13.98^{+5.02}_{-4.71}$	$16.47^{+8.06}_{-4.49}$	$10.85^{+4.39}_{-3.74}$	$16.12^{+3.78}_{-5.99}$	$23.93^{+4.98}_{-10.10}$
$n_{et}(10^{11} \text{ cm}^{-3} \text{ s})$	$0.69^{+0.33}_{-0.22}$	$0.97^{+0.27}_{-0.18}$	$1.68^{+0.56}_{-0.37}$	$1.78^{+0.69}_{-0.45}$	$2.05^{+0.47}_{-0.54}$	$0.873^{+0.15}_{-0.11}$
$n_{\text{H}}/f^{-1/2}(\text{cm}^{-3})$...	7.40	2.72	2.03	2.23	3.53	3.46
<i>O</i>	$0.21^{+0.71}_{-0.21}$	$0.17^{+0.23}_{-0.17}$	$0.68^{+0.24}_{-0.28}$	0.3(<i>frozen</i>)	$0.67^{+0.28}_{-0.20}$	$0.22^{+0.12}_{-0.22}$
<i>Si</i>	$0.62^{+0.50}_{-0.37}$	$0.56^{+0.22}_{-0.16}$	$0.31^{+0.08}_{-0.14}$	$0.94^{+0.45}_{-0.27}$	$0.45^{+0.17}_{-0.07}$	$0.35^{+0.11}_{-0.10}$
<i>S</i>	$0.86^{+0.98}_{-0.74}$	$0.64^{+0.32}_{-0.29}$	$0.61^{+0.23}_{-0.23}$	$0.92^{+0.42}_{-0.33}$	$0.93^{+0.32}_{-0.13}$	$0.28^{+0.20}_{-0.10}$
<i>Fe</i>	$1.00^{+1.00}_{-0.41}$	$0.56^{+0.18}_{-0.12}$	$0.67^{+0.17}_{-0.14}$	$0.85^{+0.34}_{-0.21}$	$0.73^{+0.37}_{-0.13}$	$0.57^{+0.13}_{-0.10}$

3.2 The shell regions

The X-ray spectra of the shell regions S1-S5 have at least two components. Both the double-*vpshock* model and *vpshock* + *powerlaw* model fit the X-ray spectra of these regions well.

In the double-*vpshock* case, the high ionization timescale $n_{et} (\geq 10^{12} \text{ cm}^{-3} \text{ s})$ of the cool components indicates that the cool gas has approached or been in the ionization equilibrium. However, the ionization age derived for the shocked gas seems too large. Taking S3 for example, we estimate the ionization age $t \approx 3 \times 10^5 f^{1/2} \text{ yr}$. The kinematic age of N132D is 3150 ± 200 years (Morse et al., 1995). Unless the filling factor is as small as 10^{-4} , the ionization age will be too old to understand. On the other hand, the outer shell is commonly considered to be swept-up ISM. Therefore the co-existence of two thermal components along the shell is difficult to explain. One possibility is that the regions we selected to obtain sufficient counts statistics are quite large in physical extent and contain emission from gas at varying thermodynamic states.

Table 3

POWERLAW+VPSHOCK fitting results with 90% confidence ranges and estimates of the gas density for regions S1-S6

Region	S1	S2	S3	S4	S5	S6
$N_{\text{H}}(10^{21} \text{ cm}^{-2})$	$1.8^{+0.3}_{-0.5}$	$1.5^{+0.4}_{-0.4}$	$1.7^{+0.2}_{-0.2}$	$2.8^{+0.4}_{-0.2}$	$2.0^{+0.5}_{-0.4}$	$1.5^{+0.3}_{-0.3}$
net count rate						
$(10^{-2} \text{ counts s}^{-1})$	8.47 ± 0.09	14.73 ± 0.13	18.87 ± 0.14	12.64 ± 0.12	15.45 ± 0.13	17.16 ± 0.14
$\chi^2/\text{d.o.f.}$	1.15	1.75	1.53	1.41	1.17	1.65
$F^{(0)}(0.3\text{-}8 \text{ keV})$						
$(10^{-11} \text{ ergs cm}^{-2} \text{ s}^{-1})$	0.757	1.27	1.66	1.84	1.40	1.34
$V(10^{57} \text{ cm}^3)$	0.19	4.64	9.81	5.37	3.19	4.94
Powerlaw component						
$PhoIndex$	$2.57^{+0.29}_{-1.24}$	$3.09^{+0.35}_{-0.39}$	$3.05^{+0.31}_{-0.41}$	$3.40^{+0.22}_{-0.26}$	$2.83^{+0.45}_{-0.22}$	$2.37^{+0.45}_{-0.24}$
$norm(10^{-4})$	$0.67^{+1.22}_{-0.56}$	$2.94^{+2.36}_{-1.78}$	$5.53^{+3.34}_{-2.48}$	$8.23^{+3.06}_{-1.28}$	$3.51^{+3.89}_{-1.78}$	$1.52^{+1.57}_{-0.76}$
Thermal component						
$kT_x(\text{keV})$	$0.60^{+0.04}_{-0.04}$	$0.54^{+0.04}_{-0.07}$	$0.65^{+0.02}_{-0.02}$	$0.54^{+0.07}_{-0.05}$	$0.61^{+0.02}_{-0.04}$	$0.60^{+0.02}_{-0.01}$
$norm(10^{-4})$	$43.21^{+10.51}_{-8.94}$	$68.26^{+19.90}_{-14.89}$	$71.15^{+13.15}_{-13.03}$	$62.11^{+17.41}_{-15.47}$	$72.94^{+12.59}_{-15.60}$	$89.93^{+6.43}_{-11.92}$
$n_e t(10^{11} \text{ cm}^{-3} \text{ s})$	$5.91^{+10.74}_{-3.00}$	$7.93^{+5.34}_{-2.94}$	$9.95^{+8.58}_{-4.20}$	$4.93^{+2.43}_{-1.46}$	$20.53^{+12.94}_{-11.84}$	$15.5^{+13.15}_{-7.65}$
$n_{\text{H}}/f^{-1/2}(\text{cm}^{-3})$...	23.36	6.03	4.24	5.35	7.52	6.71
O	$0.36^{+0.24}_{-0.14}$	$0.44^{+0.29}_{-0.13}$	$0.73^{+0.36}_{-0.11}$	$0.42^{+0.20}_{-0.12}$	$0.81^{+0.39}_{-0.26}$	$0.53^{+0.12}_{-0.16}$
Ne	$0.49^{+0.21}_{-0.12}$	$0.65^{+0.19}_{-0.13}$	$1.06^{+0.23}_{-0.18}$	$1.18^{+0.45}_{-0.30}$	$1.25^{+0.41}_{-0.28}$	$0.61^{+0.17}_{-0.14}$
Si	$0.35^{+0.13}_{-0.10}$	$0.46^{+0.14}_{-0.11}$	$0.32^{+0.11}_{-0.09}$	$0.79^{+0.30}_{-0.20}$	$0.38^{+0.08}_{-0.05}$	$0.25^{+0.07}_{-0.06}$
S	$0.63^{+0.41}_{-0.38}$	$0.92^{+0.41}_{-0.40}$	$0.88^{+0.31}_{-0.29}$	$2.17^{+0.59}_{-0.67}$	$1.31^{+0.40}_{-0.34}$	$0.34^{+0.21}_{-0.19}$
Fe	$0.37^{+0.10}_{-0.06}$	$0.33^{+0.08}_{-0.05}$	$0.36^{+0.11}_{-0.07}$	$0.31^{+0.11}_{-0.07}$	$0.32^{+0.11}_{-0.05}$	$0.31^{+0.05}_{-0.03}$

In the *vpshock+powerlaw* case, the spectra provide a possibility for the non-thermal component to be present along the shell. Although the theories of X-ray synchrotron emission from SNR shell still have open questions, more and more shell-like SNRs have been confirmed to exhibit X-ray synchrotron emission. Two shell-like SNRs, SN 1006, and G347.3-0.5, are found to be dominated by synchrotron X-rays with no emission line (Koyama et al., 1995; Koyama et al., 1997; Slane et al., 1999) while some shell-like SNRs such as Cas A, Kepler, Tycho, and RCW86 are predominantly thermal but contain a hard energy tail due to electron synchrotron. Like these SNRs, N132D is young and has a shell-like morphology. It is thus interesting to find a hard energy tail in the shell of N132D. The presence of X-ray synchrotron may be helpful in understanding the positional coincidence of the X-ray shell with the radio one (Dickel & Milne, 1995). The best-fit photon indices we derived are between 2.3 and 3.4 which are consistent with the typical value (2.5-3) for diffuse shock acceleration in those shell-like SNRs (Ballet, 2006). If the non-thermal component could be further confirmed, N132D would be listed as another X-ray synchrotron SNR. The slightly enhanced element abundances in some portions of the shell might be ascribed to the dust destruction by sputtering.

3.3 The ridge

The ridge region S6 shows some consistency with the shell regions S1-S5. In morphology, the ridge connects the shell at the south. In spectra, the parameters of S6 derived from the two models are similar to those of S1-S5 except for some lower element abundances. The Spitzer images show that both the ridge and the shell have strong $24\mu m$ emission which is from swept-up, shock-heated dust grains (Tappe et al., 2006). So we suggest that the ridge region S6 may be the projection of a part of shell in which the ISM is the primary ingredient.

4 Conclusion

Using the zeroth-order data of Chandra HETG observation, we tentatively performed a spatially-resolved X-ray spectroscopy study of SNR N132D. The EW maps of O, Ne, Mg, Si, and S are generated. The faint interior regions have lower density, higher temperature above 1keV than that of bright interior regions. The X-ray spectra along the shell can be phenomenally described with either a double-*vpshock* model or a *vpshock* + *powerlaw* model. For the double-*vpshock* case, the low temperature component has a unreasonable high ionization timescale, and two thermal components along the shell as swept-up ISM are difficult to understand. For the *vpshock* + *powerlaw* model, Ne and S are slightly overabundant in some regions of the shell, and the best-fit photon indices of the non-thermal component are between 2.3 and 3.4, consistent with diffuse shock acceleration. If the non-thermal component is true, N132D would be listed as another TeV particle acceleration laboratory.

We thank the two anonymous referees for a thorough review of this work and for useful comments. We also thank Yang Su and Jiang-Tao Li for technical assistance. Y.C. acknowledges support from NSFC grants 10221001 and 10673003.

References

- Ballet, J. X-ray synchrotron emission from supernova remnants. *AdSpR.* 37, 1902, 2006.
- Behar, E., Rasmussen, A. P., Griffiths, R. G., Dennerl, K., Audard, M., Aschenbach, B., Brinkman, A. C. High-resolution X-ray spectroscopy and imaging of supernova remnant N132D. *Astron. Astrophys.* 365, L242–L247, 2001.
- Blair, W. P., Raymond, J. C., Long, K. S. IUE spectra and optical imaging of the oxygen-rich supernova remnant N132D. *Astrophys. J.* 423, 334–343, 1994.

Blair, W. P., Morse, J. A., Raymond, J. C., Kirshner, R. P., Hughes, J. P., Dopita, M. A., Sutherland, R. S., Long, K. S., Winkler, P. F. Hubble Space Telescope Observations of Oxygen-rich Supernova Remnants in the Magellanic Clouds. II. Elemental Abundances in N132D and 1E 0102.2-7219. *Astrophys. J.* 537, 667–689, 2000.

Canizares, C. R., Flanagan, K. A., Davis, D. S., Dewey, D., Houck, J. C. High Resolution Spectroscopy of Two Oxygen-Rich SNRs with the Chandra HETG. *ASPC.* 234, 173–180, 2001.

Chen, Y., Zhang, F., Williams, R. M., Wang, Q. D. Supernova Remnant Crossing a Density Jump: A Thin-Shell Model. *Astrophys. J.* 595, 227, 2003.

Danziger, I. J. & Dennefeld, M. Supernova ejecta in the Large Magellanic Cloud. *Astrophys. J.* 207, 394–407, 1976.

Dickel, J. R. & Milne, D. K. Radio properties of three young supernova remnants in the Large Magellanic Cloud. *Astron. J.* 109, 200–208, 1995.

Favata, F., Vink, J., Parmar, A. N., Kaastra, J. S. Mineo, T. BeppoSAX LECS/MECS X-ray spectroscopy of the young supernova remnant N132D. *Astron. Astrophys.* 324, L45–L48, 1997.

Favata, F., Vink, J., Parmar, A. N., Kaastra, J., Mineo, T. Erratum: BeppoSAX LECS/MECS X-ray spectroscopy of the young supernova remnant N132D. *Astron. Astrophys.* 340, 626, 1998.

Hughes, J. P. X-ray studies of the supernova remnant N132D. I - Morphology. *Astrophys. J.* 314, 103–110, 1987.

Hughes, J. P., Hayashi, I., Koyama, K. ASCA X-Ray Spectroscopy of Large Magellanic Cloud Supernova Remnants and the Metal Abundances of the Large Magellanic Cloud. *Astrophys. J.* 505, 732–748, 1998.

Hwang, U., Hughes, J. P., Canizares, C. R., Markert, T. H. High-resolution X-ray spectroscopy of the supernova remnant N132D. *Astrophys. J.* 414, 219–229, 1993.

Hwang, U., Holt, S. S., Petre, R. Mapping the X-Ray-emitting Ejecta in Cassiopeia A with Chandra. *Astrophys. J.* 537, L119–L122, 2000.

Koyama, K., Petre, R., Gotthelf, E. V., Hwang, U., Matsuura, M., Ozaki, M., Holt, S. S. Evidence for Shock Acceleration of High-Energy Electrons in the Supernova Remnant SN:1006. *Nature.* 378, 255–258, 1995.

Koyama, K., Kinugasa, K., Matsuzaki, K., Nishiuchi, M., Sugizaki, M., Torii, K., Yamauchi, S., Aschenbach, B. Discovery of Non-Thermal X-Rays from the Northwest Shell of the New SNR RX J1713.7-3946: The Second SN 1006?. *PASJ.* 49, L7–L11, 1997.

Lasker, B. M. Studies of N132D, a supernova remnant similar to Cassiopeia A in the large Magellanic cloud. *Astrophys. J.* 223, 109–121, 1978.

Mathewson, D. S., Ford, V. L., Dopita, M. A., Tuohy, I. R., Long, K. S., Helfand, D. J. Supernova remnants in the Magellanic Clouds. *Astrophys. J.S.* 51, 345–355, 1983.

Morrison, R. & McCammon, D. Interstellar photoelectric absorption cross sections, 0.03-10 keV. *Astrophys. J.* 270, 119–122, 1983.

Morse, J. A., Winkler, P. F., Kirshner, R. P. Spatially Resolved Kinematics and Longslit Spectroscopy of the Young, Oxygen-Rich Supernova Remnant N132D in the Large Magellanic Cloud. *Astron. J.* 109, 2104–2120, 1995.

Morse, J. A., Blair, W. P., Dopita, M. A., Hughes, J. P., Kirshner, R. P., Long, K.

S., Raymond, J. C., Sutherland, R. S., Winkler, P. F. Hubble Space Telescope Observations of Oxygen-Rich Supernova Remnants in the Magellanic Cloud. I. Narrow-Band Imaging of N132D in the LMC. *Astrono. J.* 112, 509–533, 1996.

Russell, S. C., Dopita, M. A. Abundances of the heavy elements in the Magellanic Clouds. III - Interpretation of results. *Astrophys. J.* 384, 508–522, 1992.

Slane, P., Gaensler, B., Dame, T. M., Hughes, J. P., Plucinsky, P. P., Green, A. Nonthermal X-Ray Emission from the Shell-Type Supernova Remnant G347.3-0.5. *Astrophys. J.* 525, 357–367, 1999.

Tappe, A., Rho, J., Reach, W. T. Shock Processing Of Interstellar Dust And Polycyclic Aromatic Hydrocarbons In The Supernova Remnant N132D. *Astrophys. J.* 653, 267, 2006.